
Article:
Xiao, P., Tian, X., Liu, M. et al. (1 more author) (2019) Multipath smearing suppression for synthetic aperture radar images of harbor scenes. IEEE Access. p. 1. ISSN 2169-3536

https://doi.org/10.1109/access.2019.2897779

IEEE Access
Multidisciplinary | Rapid Review | Open Access Journal

Date of publication xxxx 00, 0000, date of current version xxxx 00, 0000.

Digital Object Identifier 10.1109/ACCESS.2018.Doi Number

Multipath Smearing Suppression for Synthetic Aperture Radar Images of Harbor Scenes

Peng Xiao [1], Xiaolu Tian [2], Min Liu [1], and Wei Liu [3], Senior Member, IEEE

[1]Qian Xuesen Laboratory of Space Technology, China Academy of Space Technology, Beijing, 100094 China
[2]Space Star Technology Co., Ltd., Beijing, 100086 China
[3]Portobello Center Communications Research Group, Department of Electronic & Electrical Engineering, University of Sheffield, Sheffield S1 4ET, United Kingdom

Corresponding author: Peng Xiao (e-mail: xiaopeng@qxslab.cn)

This work was supported in part by the Innovation Workstation of Qian Xuesen Lab.

ABSTRACT Due to the periodic and non-periodic variations in the sea surface, smearing is caused by the multiple paths between the sea surface and man-made objects in synthetic aperture radar images of harbor areas. This smearing can cover the real targets and lead to false alarms. To derive the relationship between the motion of the sea surface and blurring in synthetic aperture radar images, a sway signal model is established, and the Doppler spectrum of the sea surface is found to undulate for well-focused targets with different shapes. Based on this finding, a subaperture combined detection algorithm based on an inverse coherence factor filter is developed to separate the unwanted pixels from the resultant synthetic aperture radar image. An energy balance is used to suppress interference and maintain the resolution of the real scene. The algorithm can be automatically applied to synthetic aperture radar images. The experimental results with TerraSAR-X spotlight mode data show that this method can effectively detect and mitigate the effects of time-varying multipath phenomena.

INDEX TERMS Azimuth smearing suppression, Radar signal processing, Synthetic aperture radar, Radar imaging, Interference suppression, Sea measurements, Sea coast, Radar remote sensing

I. INTRODUCTION

Synthetic aperture radar (SAR) provides an effective remote sensing technology for collecting images of ocean scenes in cloudy weather. A basic assumption of SAR is that the value of the scattering coefficient for cells of a given resolution must be held constant during the observation process; otherwise, the target may be out of focus in the final imaging result. However, in marine environments, there are many time-varying objects, such as ships and sea waves, which lead to unexpected distance changes. If the residual product of distance phase compensation exceeds a quarter of π during the observation process, the scatterer will produce a blurred product. As a result, for several seconds in synthetic aperture time, smearing occurs in the images of harbor scenes, resulting in a "dirty" image [1], [2]. The blurred shore and vessels may reduce the value of remote sensing images.

The motion of scatterers can be divided into translation and sway submotions (which lead to complex periodic variations of distance). The former is common and related to the active movement of carriers, such as ships and automobiles. This form of motion is often considered uniform linear motion (ULM). ULM blur has been widely discussed in the literature, and the refocusing problem has been effectively solved [3].

In this paper, we focus on another type of smearing that results from the interactions between sea waves and strong scatterers. Micro-Doppler effects caused by small complex variations in the sea surface height normally lead to short lines that appear along the edges of man-made objects and cover the real targets. If the reflection paths can be accurately detected or estimated in a stable and simple environment, one can reconstruct the sparse targets and effectively suppress the discrete "ghost" targets [4]-[10]. Another method of resolving such issues involves using massive multiple input and multiple output (MIMO) antenna arrays [11]-[13] that cannot be installed on satellites. However, the unpredictable variations in the sea surface result in irregular distance changes over time. The above methods based on inverse solutions are not suitable for mitigating this specific phenomenon. Thus, it is difficult to suppress smearing in

harbor scenes, accurately predict motion characteristics and remove the smearing associated with variable winds.

Although temporal variations in the sea surface complicate these issues, micro-Doppler information can still be used to address the smearing problem. The micro-Doppler signatures of waves vary over time due to smearing effects and differ from those of well-focused target. In this paper, we develop a smearing filter based on an inverse coherence factor (ICF) that can remove the abnormal time-varying pixels and noise from the complex harbor background. Furthermore, an energy balance is used to suppress interference and maintain the resolution of the real scene influenced by smearing.

In Sections II and III, we analyze the signals of blurred objects in a harbor area and propose a hypothesis that the Doppler spectrum of smearing is discontinuous and undulating, as verified with SAR data. In section IV, we discuss how to detect and suppress smearing in complex images. Experimental results with real data are provided in Section V to evaluate the performance of the developed method, and conclusions are drawn in Section VI.

II. PHENOMENA LEADING TO SMEARING

Since the water surface can reflect electromagnetic waves, the multiple paths between the sea and the man-made objects on it can lead to very strong scattering. As shown in Figure 1, the scatterers on the sea surface move reciprocally because of the movement of ocean waves. If the motion is random and complex, phase compensation may fail, leading to defocusing, which yields many short lines along edges.

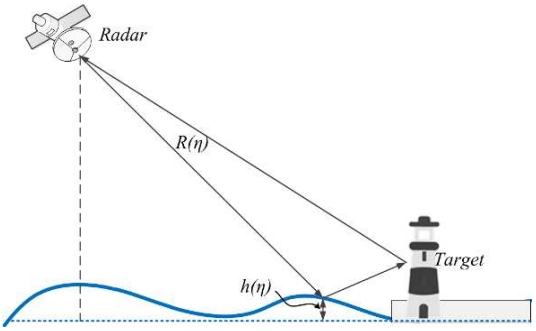

FIGURE 1. Scatterers on the sea surface are influenced by wave motion

The maximum synthetic aperture time of existing SAR satellites is less than 10 seconds (for example, the spotlight mode of TerraSAR-X is approximately 7 seconds); therefore, the effect of the swaying motion of waves on SAR images mainly comes from wind waves based on the convenient classification of the wave period [14].

A two-scale model is normally used to represent the sea surface as an approximation, where multiplicative noise and flow effects are combined [15], as shown in Figure 2. In this case, k is the wavenumber of sea waves. Bragg scattering encompasses the subtle fluctuations in the waves, which can be considered frozen noise. Long waves represent the large-scale variations. The rough cut-off point is the reciprocal of the spatial resolution $2\pi/\rho$. Therefore, multipath smearing is mainly caused by long waves.

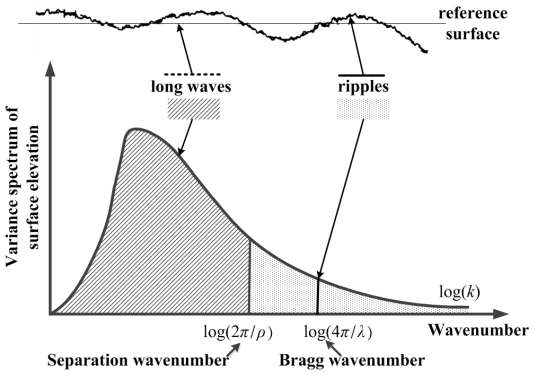

FIGURE 2. Two-scale model of the sea surface. The long wave scale leads to texture and defocusing issues in SAR ocean imagery, and the ripples create additional noise.

In reality, for finite values of the wave amplitude (height), the particle paths are slightly displaced from their previous positions after the passage of each crest, a phenomenon known as Stokes drift [16]. The free surface elevation $h(x,\eta)$ of one wave component is sinusoidal and a function of the horizontal position x and time η:

$$h(x,\eta) = A_s \cos\left(\frac{2\pi}{\lambda_s}x - 2\pi f_s \eta\right) \tag{1}$$

where A_s and f_s are the wave amplitude and frequency, respectively, and λ_s is the wavelength.

For a specific position x_0, the surface elevation is simplified as follows.

$$h(\eta) = A_s \cos(2\pi f_s \eta + \phi_0) \tag{2}$$

Long waves can be seen as the superposition of several single-frequency waves from a narrow spectrum.

$$H(\eta) = \sum_{i=1}^{K} h_i(\eta) = \sum_{i=1}^{K} A_i \cos(2\pi f_i \eta + \phi_i) \tag{3}$$

The relationship between A_s and f_s can be determined by actual measurements. A simple empirical power spectrum called the Pierson-Moskowitz (P-M) spectrum was proposed in [17]. This spectrum is generally accepted at low angular frequencies ω_s:

$$S(\omega_s) = \frac{\alpha}{\omega_s^5}\exp\left[-\beta\left(\frac{g}{v_w \omega_s}\right)^4\right] \tag{4}$$

where v_w is the wind speed ten meters above the sea surface, α and β are empirical constants, g is gravitational acceleration, $\omega_s = 2\pi f_s$ and $S(\omega_s) = \pi A_s^2$. As reported by the ITTC (International Towing Tank Conference) in 1972 [17], $\alpha = 0.78$ and $\beta = 1.25$. The spectrum reaches its peak $S(\omega_m)$ when $\omega_s = g/v_w$ and rapidly declines. The equivalent pass band is as follows.

$$B_e = \frac{\int_0^\infty S(\omega_s)\,d\omega_s}{S(\omega_m)} \approx 0.06\omega_m \tag{5}$$

Hence, the above spectrum can be seen as a narrow band system, and the frequency of the wave group $f_m = \omega_m / 2\pi$ provides the main contribution. The swell has a frequency spectrum with a similar shape. As waves disperse further without wind, the swell spectrum becomes narrower, sometimes reaching 7% or less of the peak. Thus, the swell has lost some amount of randomness and has a more defined shape and direction. Therefore, swell models (3) are often similar to long-peak and low-frequency sine waves [19].

III. SIGNAL MODELS

In the classic SAR echo model, it is assumed that the scatterers are stationary and the radar moves in a controllable way. The signal with pulse compression for a point target is described as follows [20]:

$$\begin{aligned} S_0(\tau,\eta) &= A_0 \sin c\left[\tau - 2R(\eta)/c\right] \\ &\quad \times W(\eta)\exp\left\{-j2\pi \times 2R(\eta)/\lambda\right\} \end{aligned} \tag{6}$$

where A_0 is the backscattering coefficient of the target, τ is fast time (range time), η is slow time (azimuth time), c is the speed of light in free space, $W(\eta)$ is the azimuth weight (related to the antenna radiation pattern), λ is the wavelength of the carrier frequency, and $2R(\eta)$ is the instantaneous transmission distance, which is adjusted based on azimuth compression.

In the context of SAR imaging, the elevation component is projected onto the range component based on a time delay. Thus, the reduction in image quality is mainly caused by the range component, as shown in Figure 3. With incidence angle θ_i, $\Delta R(\eta)$ is caused by cosine function elevation variations.

$$\begin{aligned} \Delta R(\eta) &\approx h(\eta)\cos\theta_i \\ &= A_s \cos\theta_i \cos\left(2\pi f_s \eta + \phi_0\right) \\ &= A_r \cos\left(2\pi f_s \eta + \phi_0\right) \end{aligned} \tag{7}$$

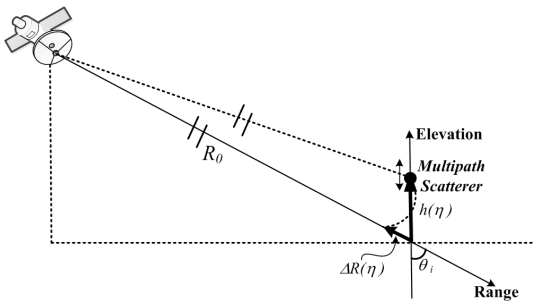

FIGURE 3. The elevation component is mapped to the range component based on a time delay.

For a stationary target, the distance history is approximated as follows:

$$R(\eta) = \sqrt{R_0^2 + V_r^2 \eta^2} + \frac{\lambda}{6}\gamma(R_0)\eta^3 \tag{8}$$

where R_0 is the closest distance, V_r is the equivalent flying speed, and $\gamma(R_0)$ is an additional cubic coefficient that has no analytic expression [21]. Azimuth processing can compensate for the phase caused by $R(\eta)$ and provide a high-resolution image.

Suppose that the displacement of scatterers in the range direction for slow time is $\Delta R(\eta)$. The instantaneous distance then takes the following form.

$$R_s(\eta) = \sqrt{\left[R_0 + \Delta R(\eta)\right]^2 + V_r^2 \eta^2} + \frac{\lambda}{6}\gamma(R_0)\eta^3 \tag{9}$$

For a swell wave, the frequency of the swell is 0 Hz $\le f_s \le$ 3 Hz, and the amplitude A_s is related to the wave height, which may be several meters or less. For a low Earth orbit (LEO) satellite platform, V_r / R_0 is always less than 0.01 Hz. Hence, the distance history with swell motion can be simplified as follows [22].

$$\begin{aligned} R_s(\eta) &\approx R(\eta) + \Delta R(\eta) \\ &\approx R(\eta) + A_r \cos\left(2\pi f_s \eta + \phi_0\right) \end{aligned} \tag{10}$$

The time-frequency relationship for cosine motion is given by the following equation.

$$\begin{aligned} f_w(\eta) &= -\frac{2}{\lambda}\frac{dR_s(\eta)}{d\eta} \\ &= -\frac{2}{\lambda}\left[\frac{dR(\eta)}{d\eta} - 2\pi f_s A_r \sin\left(2\pi f_s \eta + \phi_0\right)\right] \end{aligned} \tag{11}$$

Ignoring the cubic error, the azimuth-focused result $f_{wo}(\eta)$ is as follows:

$$\begin{cases} f_{wo}(\eta) = f_{ref}\left(\eta_{ref}\right) = f_w\left(\eta_w\right) \\ \eta = \eta_w - \eta_{ref} \end{cases} \tag{12}$$

where $f_{ref}(\eta)$ is the time-frequency relationship for the reference target, which is assumed to be stationary.

$$f_{ref}(\eta) = -\frac{2}{\lambda}\frac{dR(\eta)}{d\eta} \tag{13}$$

The azimuth-focused result $f_{wo}(\eta)$ is simplified as follows:

$$f_{wo}(\eta) \approx \frac{V_r^2}{\pi f_s \lambda R_0}\left[2\pi f_s \eta + \phi_0 - \arcsin\left(\frac{V_r^2 \eta}{2\pi f_s A_r R_0}\right)\right] \tag{14}$$

where $\arcsin(x)$ is not limited to the range $[-\pi/2, \pi/2]$. As shown in Figure 4, multiple varying paths can result in a defocusing effect.

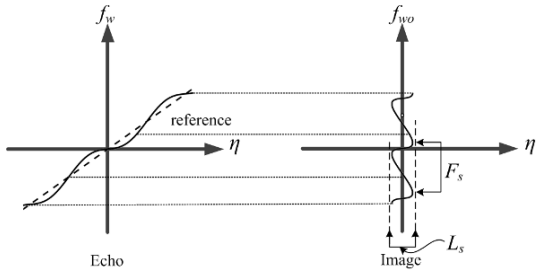

FIGURE 4. The Doppler spectrum of sinusoidal motion. The dotted line in the echo is the focus reference, and the solid line is shifted during imaging.

If the synthetic aperture time T_a and processing bandwidth B_a are both sufficiently large, the defocusing

limit in the azimuth direction L_s and period F_s are as follows.

$$L_s = \frac{4\pi f_s A_r R_0}{V_r^2} \tag{15}$$

$$F_s = \frac{2V_r^2}{f_s \lambda R_0} \tag{16}$$

To verify the above derived results, point scatterer simulations based on the parameters in Table I are shown in Figure 5 for different wave amplitudes A_r and frequencies f_s in the range direction. The length of smearing satisfies the requirements of the theoretical calculation (15).

TABLE I
PARAMETERS USED IN THE SIMULATIONS

Symbol	Parameter name	Value	Units
f_0	Radar frequency	9.65	GHz
θ_i	Incidence angle	35	deg
R_0	Slant range to center	616.34	km
B_r	Range bandwidth	300	MHz
B_a	Azimuth bandwidth	38.29	kHz
PRF	Pulse repetition frequency	4408.14	Hz
V_r	Equivalent speed	7075	m/s
T_a	Synthetic aperture time	7.30	s

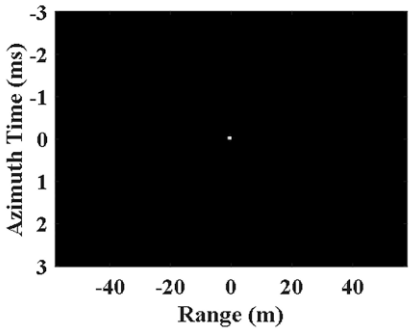

(a) Stationary point scatterer

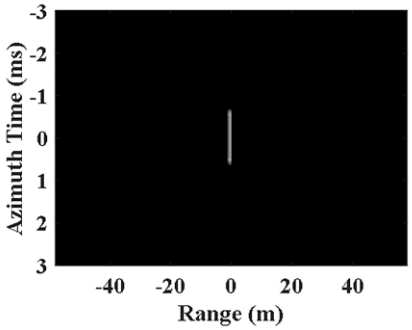

(b) Amplitude 7.4 cm, frequency 0.1 Hz, and smearing 1.1 ms

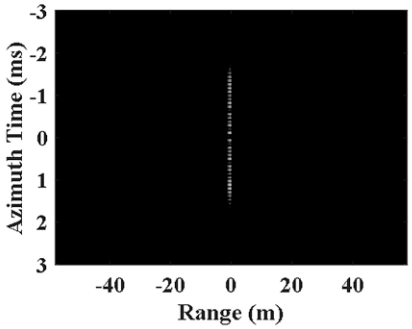

(c) Amplitude 3.7 cm, frequency 0.46 Hz, and smearing 2.6 ms

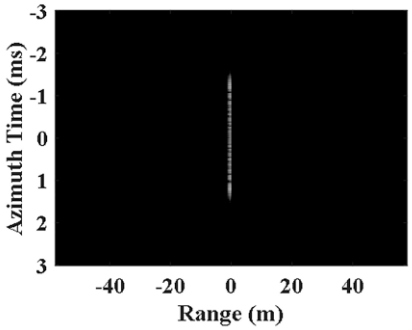

(d) Amplitude 7.4 cm, frequency 0.23 Hz, and smearing 2.6 ms

FIGURE 5. Point scatterer simulations of smearing. The length of smearing is related to the amplitude and frequency of wave.

In this study, we select a representative scene, as shown in Figure 6a. The scene was observed by TerraSAR-X in spotlight mode. The image was captured over Lvshun, China, on 14 December 2014, with the same parameters as shown in Table I.

As shown by the optical images in Figure 6(b)-(d), a man-made island was under construction, and a pontoon type breakwater surrounded the island (shown in Figure 6(c)). Clearly, many strong lines can be seen along the coast in the SAR image, but they do not exist in the optical images (shown in Figure 6(b)). Additionally, for the same wind scale (shown in Figure 6(d)), waves appear around the island. According to the abundance and positions of smearing, we can speculate that the smearing is due to the interactions between the sea surface and pontoons.

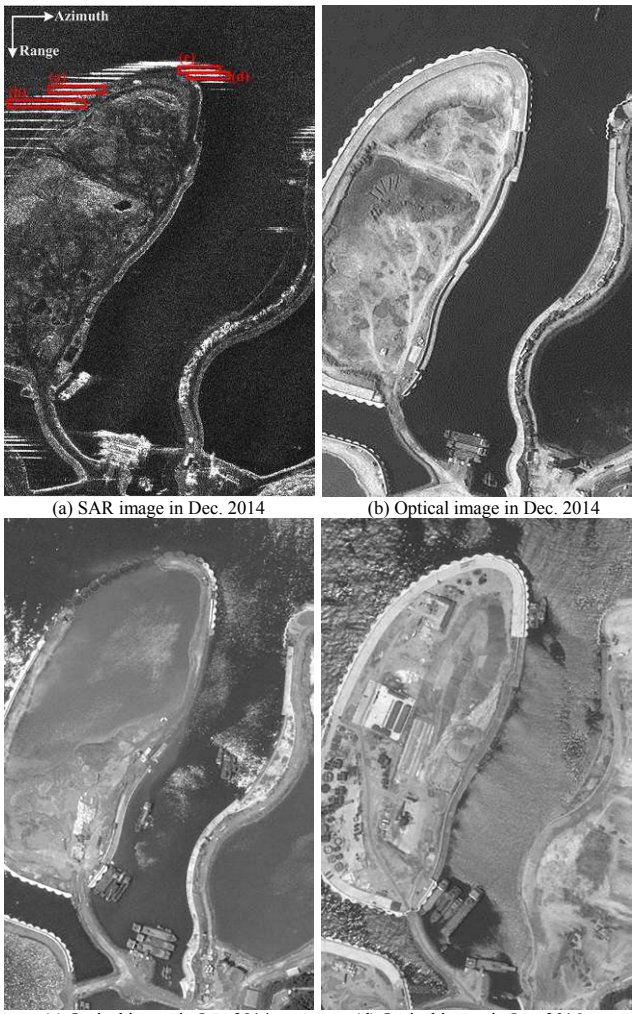

(a) SAR image in Dec. 2014 (b) Optical image in Dec. 2014

(c) Optical image in Jun. 2014 (d) Optical image in Jun. 2016

FIGURE 6. Man-made island in Lvshun China. The smearing along the island in the SAR image (a) does not exist in optical images (b), (c) and (d).

In Figure 7, four areas of smearing were chosen from Figure 6(a). With time frequency analysis, the Doppler spectra were found to satisfy the sway hypothesis presented in Figure 4.

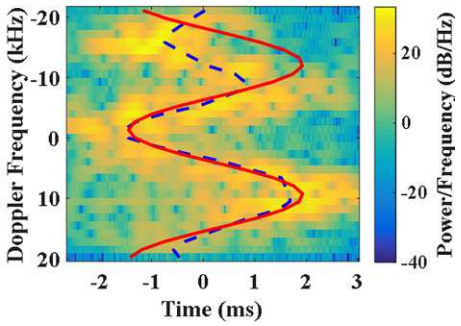

(a) Fs ≈ 21.8 kHz and Ls ≈ 3.38 ms

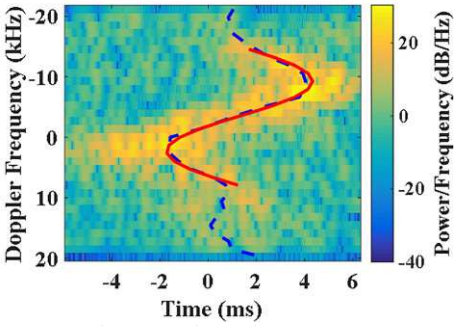

(b) Fs ≈ 23.0 kHz and Ls ≈ 6.06 ms

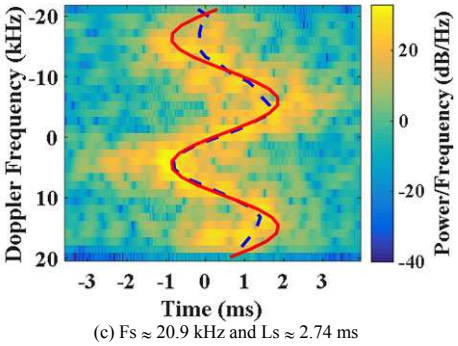

(c) Fs ≈ 20.9 kHz and Ls ≈ 2.74 ms

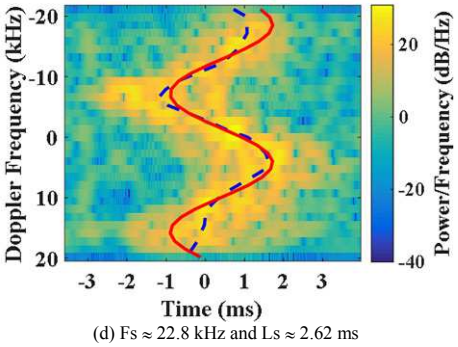

(d) Fs ≈ 22.8 kHz and Ls ≈ 2.62 ms

FIGURE 7. Time frequency analysis of the smearing in Figure 6(a). The dotted lines are peaks at the same frequency, and the red lines are the fitting results of (14).

As reported in [19], the period of waves is proportional to the wind speed $f_s^{-1} \approx 0.64\, v_w$ (s). Thus, the value of period F_s can also be used to estimate the wind speed.

$$v_w = \frac{\lambda R_0}{1.28 V_r^2} F_s \tag{17}$$

The mean value of fitted F_s in the four images in Figure 7 is 22.13 kHz. Using (17), v_w should be approximately 6.60 m/s. According to the weather report on that day, the wind scale is four (v_w is between 5.5 m/s and 7.9 m/s), which is in agreement with the estimated result.

IV. DETECTION AND SUPPRESSION OF SMEARING

As shown in Figure 4 and Figure 7, the Doppler spectra of smearing are discontinuous and undulating over a short time with a very different shape compared to the well-focused spectra. For submeter systems, the discontinuous characteristic is even more remarkable because the residual

deformation of range migration correction may span several range gates. Based on this feature, there are two approaches for multipath suppression [23].

a) Micro-Doppler removal based on L-statistics (MDL), in which the 1-D signal of an SAR image in the azimuth direction is transmitted by complex short-time Fourier transform (STFT), and the micro-Doppler signal can be detected and separated by a dynamic threshold decision with L-statistics [22]

b) Coherence factor filtering (CF) [24], which measures the coherence of signals scattered from a general point, and the CF-enhanced image I_{CF} is obtained by applying the CF function to the original image I_0

$$I_{CF} = \frac{\left(\sum_{n=1}^{N} I_n\right)^2}{N\sum_{n=1}^{N} I_n^2} \times I_0 \tag{18}$$

where I_0 is partitioned into N subaperture images I_n.

The blurred objects can be effectively mitigated by both methods. However, CF misses some weak targets, and strong smearing effects remain. Additionally, MDL cannot address complex backgrounds with strong clutter, and the resolution of targets influenced by the micro-Doppler effect is reduced.

In this paper, we use the coherence factor to remove smeared pixels from the image and derive a proper threshold value to avoid speckle interference. Then, an ideal spatial filter is constructed to suppress the unwanted energy and maintain the resolution of covered real targets.

A. SUBAPERTURE COMBINED DETECTION

For an object that is divided into N subimages I_n, the ICF is as follows.

$$ICF = \frac{N\sum_{n=1}^{N} I_n^2}{\left(\sum_{n=1}^{N} I_n\right)^2} \tag{19}$$

If the Doppler spectrum of an ideal object is considered, all the I_n have the same intensity, and $ICF = 1$; otherwise, $ICF > 1$.

As shown in Figure 8, smearing clearly appears in the ICF map, which can lead to an extremely high false alarm rate. Because the speckles and noise may also lead to undulating spectra, even though there is no smearing at all, the ICF map cannot be used to directly detect smearing.

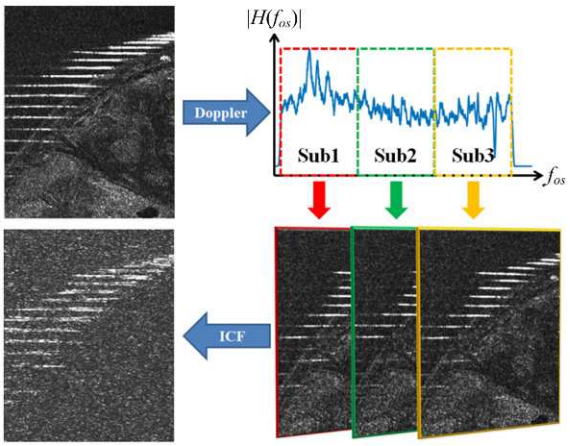

FIGURE 8. The ICF map of a smeared image.

The distribution of speckles or noise follows the subsequent equation [25].

$$P_I(I_n) = \frac{1}{\sigma}\exp\left(-\frac{I_n}{\sigma}\right) \tag{20}$$

The mean of this equation is $\overline{I_n} = \sigma$, and I_n^2 follows

$$P_I(I_n^2) = \frac{1}{2\sqrt{I_n^2}}\exp\left(-\frac{\sqrt{I_n^2}}{\sigma}\right) \tag{21}$$

with the mean value $\overline{I_n^2} = 2\sigma^2$. Thus, the ICF of a speckle can be calculated with the following formula.

$$ICF_{speckle} \approx \frac{N\left(N\overline{I_n^2}\right)}{\left(N\overline{I_n}\right)^2} = 2 \tag{22}$$

Therefore, a threshold value $ICF = 2$ can be used to remove smearing and ignore speckle interference. For a better result, a median filter can be used to remove isolated points because a clearly defocused object always encompasses three or more consecutive cells of a given resolution (as shown in Figure 9).

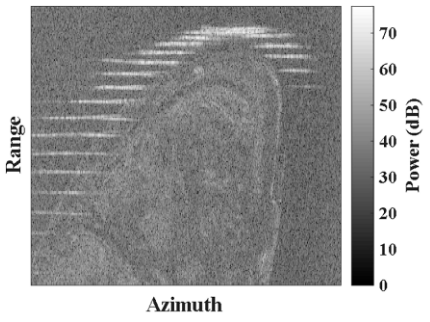

(a) An island covered by smearing

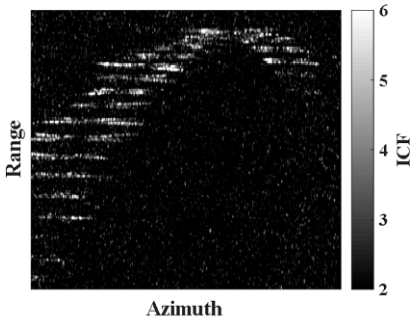

(b) Smearing filtering result

FIGURE 9. Smearing filter with subaperture combined detection.

B. SUPPRESSION OF SMEARING

Our aim is to suppress the defocused energy of smearing but not to refocus it (sometimes, the object does not really exist).

According to Figure 4 and Figure 7, it is likely that an area exists in the Doppler spectrum that is minimally affected by smearing. As shown in Figure 10, a sliding filter with a narrow bandwidth can be used to find this area by comparing the output energies. If the filter yields only the background subband of the spectrum, the energy of the filtering result is I_B. In addition, if the filter yields the subband influenced by multipath smearing, the energy contains two parts: the background part I_B and the multipath part I_M. The length of the sliding filter should be a quarter of the effective bandwidth of the image or smaller. Too large a window may result in missing the minimally affected (notch) area, and a too narrow a window may result in noise jamming (the selection of window length is discussed below).

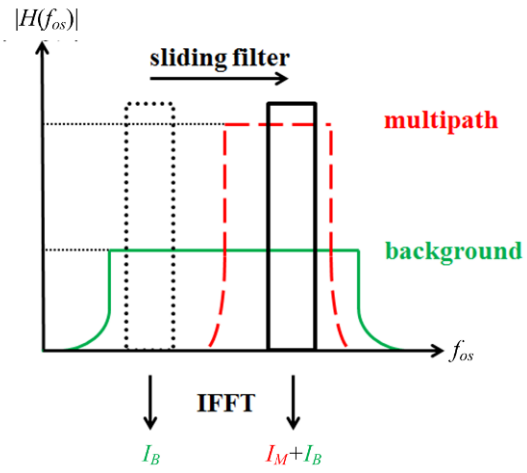

FIGURE 10. Finding the notch with a sliding filter.

If $ICF > 2$, the smearing energy is stronger than the background energy. A simple solution is to replace the interference-affected pixels with the filter results for the notch, but the resolution would be very low.

Assume that the energy of smearing is concentrated in a narrow rectangular band during a short period of time. The Doppler bandwidth of the background is divided into N parts by a sliding filter, and the smeared part is denoted as M (M may not be an integer). The ICF can be simplified to the following form.

$$ICF = \frac{N\left[M(I_B + I_M)^2 + (N-M)I_B^2\right]}{\left(NI_B + MI_M\right)^2} \tag{23}$$

The value of I_M/I_B is calculated by comparing the maximum and minimum energies of the sliding filter output results. With an ideal filter, an image with smearing suppression is obtained as follows.

$$I_{out} \approx N \times \frac{NI_B}{NI_B + MI_M} \times I_0 \tag{24}$$

The man-made island shown in Figure 6 is still used to test the effectiveness of the developed suppression method. As shown in Figure 11, the developed method performs better than MDL and CF methods. Most of the smearing effect has been effectively mitigated without significant loss of detail. However, some short lines still remain along the coast because several instances of multipath smearing overlap and a clean notch cannot be found.

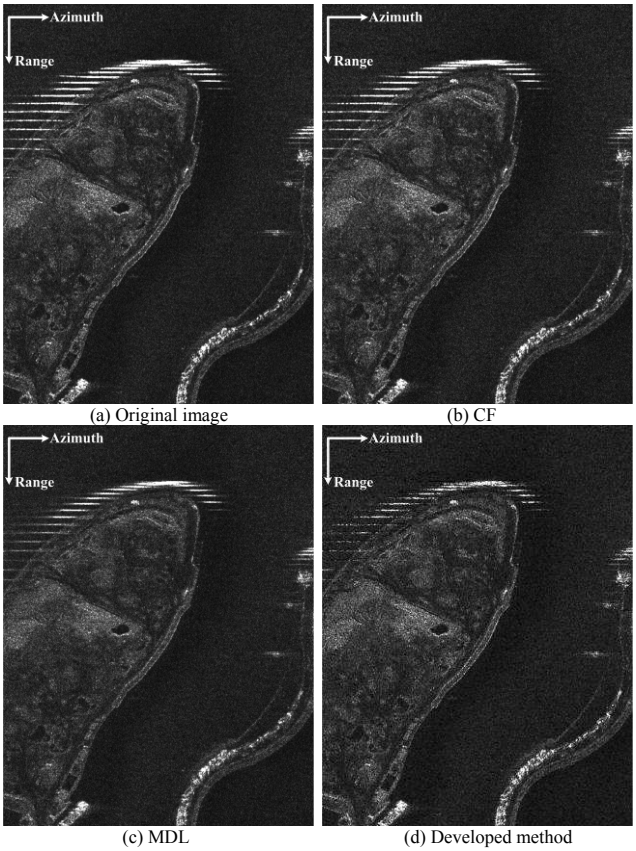

(a) Original image (b) CF

(c) MDL (d) Developed method

FIGURE 11. Multipath suppression results for the man-made island.

C. LENGTH OF THE SLIDING FILTER

Finding the notch in the Doppler spectrum is the key to the developed method. As noted, the length of the subaperture filter influences the performance of both detection and suppression.

The relationship between the azimuth resolution ρ_a and effective bandwidth B_a is as follows.

$$\rho_a = \frac{V_r}{B_a} \tag{25}$$

To facilitate the time frequency analysis, we use the time resolution in the azimuth direction.

$$t_a = \frac{\rho_a}{V_r} = \frac{1}{B_a} \tag{26}$$

Based on the length of the sliding filter ΔB, the time resolution Δt is reduced to the following form.

$$\Delta t = \frac{1}{\Delta B} \tag{27}$$

Thus, a fixed time bandwidth (TB) product is given as follows.

$$\Delta t \times \Delta B = 1 \tag{28}$$

In a discrete system, the time frequency graph of (14) is divided using a grid with intervals Δt and ΔB, and each cell crossed by the curve has an associated energy (in Figure 12).

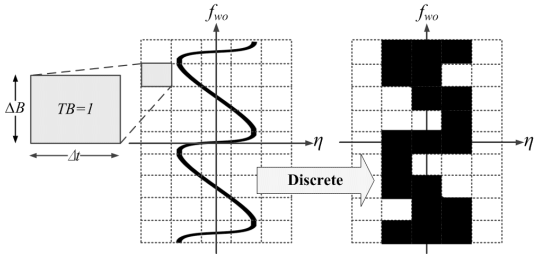

FIGURE 12. Representation of the time frequency graph. The area of each grid cell is TB = 1.

As shown in Figure 13, if the length of the sliding filter is small, the resolution cell Δt becomes too wide to filter the real targets accurately in the time domain. Conversely, if the length is big, the notch bandwidth is too narrow to be detected in the frequency domain. As shown in Figure 13(c), if the smearing is caused by a single-frequency signal, an appropriate choice of the ratio is as follows.

$$\begin{aligned}\Delta B &= f_1\left(\frac{\Delta t}{2}\right) - f_2\left(\frac{\Delta t}{2}\right) = \frac{F_s}{2}\left(1 - \frac{\Delta t}{L_s}\right) \\ &= \frac{F_s}{2}\left(1 - \frac{1}{L_s \Delta B}\right)\end{aligned} \tag{29}$$

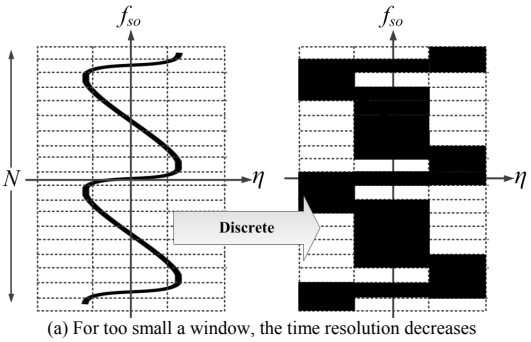

(a) For too small a window, the time resolution decreases

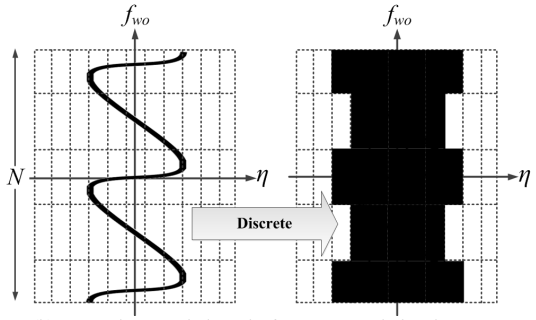

(b) For too large a window, the frequency resolution decreases

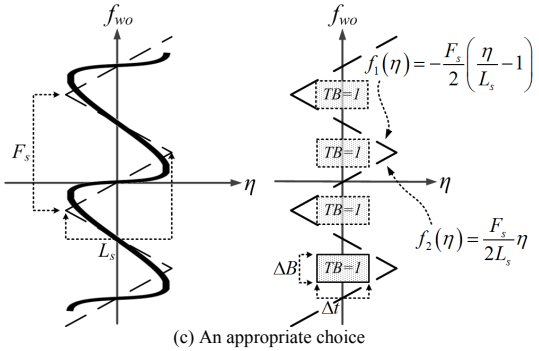

(c) An appropriate choice

FIGURE 13. Choice of the length of the sliding filter.

With (15) and (16), the optimal length of sliding filter is given as follows.

$$\begin{aligned}\Delta B(f_s) &= \frac{F_s}{4}\left(1 + \sqrt{1 - \frac{8}{F_s L_s}}\right) \\ &= \frac{V_r^2}{2 f_s \lambda R_0}\left(1 + \sqrt{1 - \frac{\lambda}{\pi A_r}}\right)\end{aligned} \tag{30}$$

Because the waves have a bandwidth signature at a specific frequency, the -20 dB power attenuation of (4) is as follows:

$$\begin{cases} S(2\pi f_{up}) = 0.01 S(2\pi f_s) \\ S(2\pi f_{down}) = 0.01 S(2\pi f_s) \end{cases} \tag{31}$$

which is considered to be far less than the peak.

By numerical calculations, we obtain the following values.

$$\begin{cases} f_{down} \approx 0.6 f_s \\ f_{up} \approx 3.2 f_s \end{cases} \tag{32}$$

To ensure that the notch can be reliably identified and filtered, the length of the sliding filter should be shortened as follows.

$$\Delta B(f_{up}) \approx \frac{V_r^2}{6 f_s \lambda R_0}\left(1 + \sqrt{1 - \frac{\lambda}{\pi A_r}}\right) \tag{33}$$

D. PERFORMANCE METRICS

The target improvement factor (TIF) is used to evaluate the performance of the developed method, and this approach is suitable for weak and non-covered targets [26]:

$$TIF = 10\log_{10}\left(\frac{\overline{I}_{out}}{\overline{I}_{in}}\right) \tag{34}$$

where $\overline{I}$ is the average smearing power.

Based on a one-dimensional simulation, the parameters of (6) and (9) are listed in Table I and are the same as those in Figure 7. In addition, the wave amplitude and frequency in the range direction are set as 0.0739 m and 0.2291 Hz, respectively, as calculated by (15) and (16) with the fitting result in Figure 7(d). We establish a point target that can be well focused in the imaging process but covered by smearing to calculate *TIF* and evaluate the performance for the real target.

The simulation results are shown in Figure 14(a). Notably, the time-frequency relationship of smearing is very similar to the results in Figure 7(d).

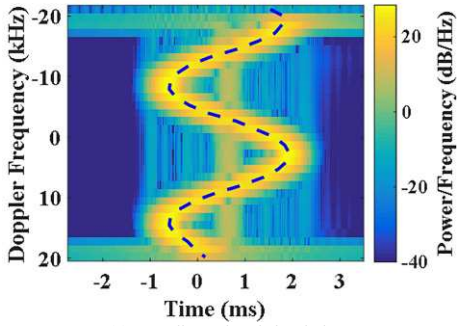

(a) One-dimensional simulation

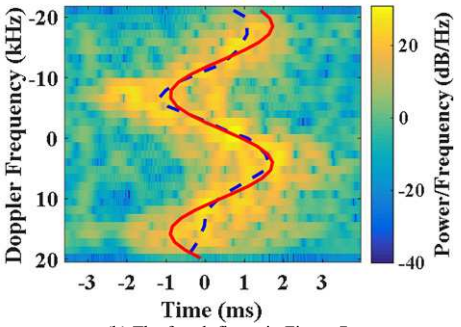

(b) The fourth figure in Figure 7

FIGURE 14. Comparison of the simulation results and measured data. The dotted lines are peaks at the same frequency, and the red line is the fitting results.

Figure 15 shows the simulation results for different subaperture numbers N.

$$N = \left\lceil \frac{B_a}{\Delta B\left(f_{up}\right)} \right\rceil \tag{35}$$

If N is too small or large, the smearing remains along the edges of the smeared region.

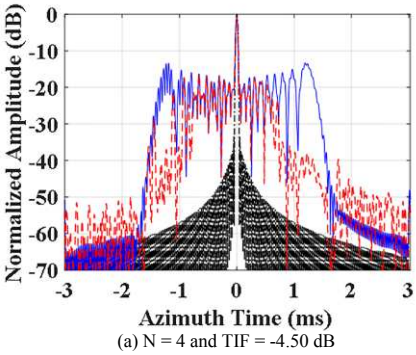

(a) N = 4 and TIF = -4.50 dB

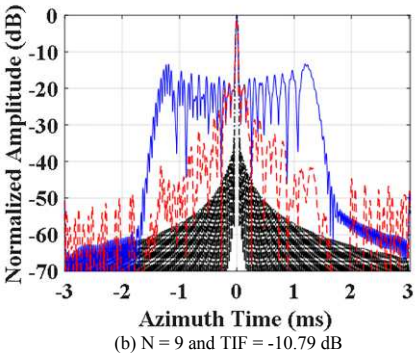

(b) N = 9 and TIF = -10.79 dB

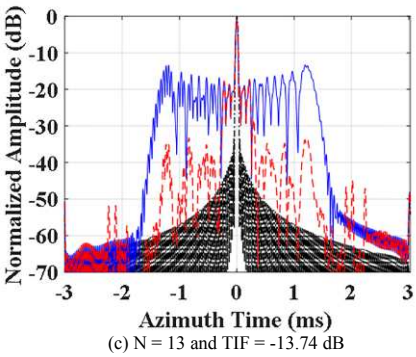

(c) N = 13 and TIF = -13.74 dB

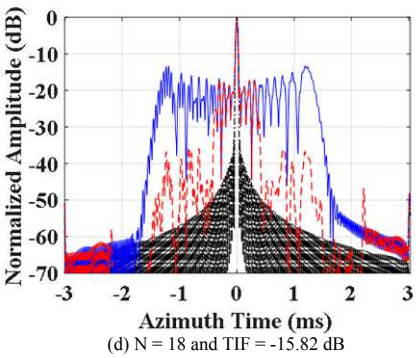

(d) N = 18 and TIF = -15.82 dB

FIGURE 15. One-dimensional simulations. The black lines represent an ideal point target, the blue lines represent smearing effects, and the red lines are the processed results.

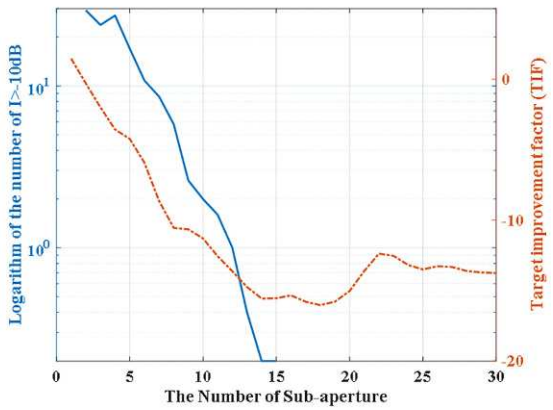

FIGURE 16. Performance curves for different subaperture numbers. The blue line is the logarithm of the number of pixels larger than -10 dB for the real target, and the red line is the TIF.

Figure 16 shows the performance curves. The blue line is the number of pixels larger than -10 dB for the real point target. If the number is much larger or smaller than 1, a failure of detection occurs. The red line is the TIF of smearing suppression. Above approximately $N = 13$, both curves reach stable states, and this finding is consistent with the results of (30) and (35).

V. EXPERIMENTS AND ANALYSES

A. POINT SCATTERER SIMULATION

A point scatterer simulation with the same parameters as listed in Table I was performed. The smearing was associated with amplitude of 3.7 cm and frequency of 0.46 Hz in the range direction. A stationary point scatterer was placed in the center of the smeared region to avoid easy detection in the imaging result.

Figure 17 shows the processed results based on different mitigation methods. CF provided no significant improvement, MDL reduces the resolution of the stationary target and IF gives the best result.

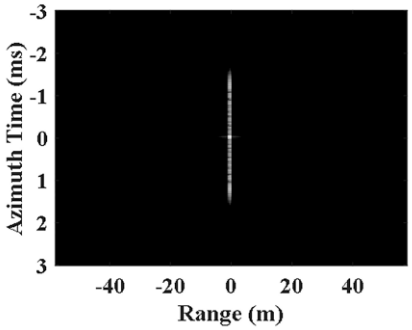

(a) Original image

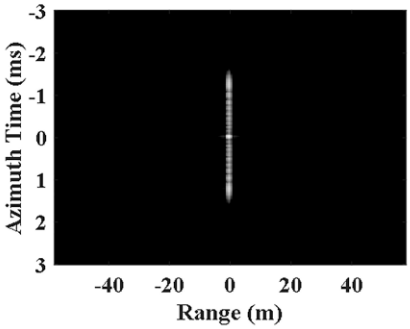

(b) CF method

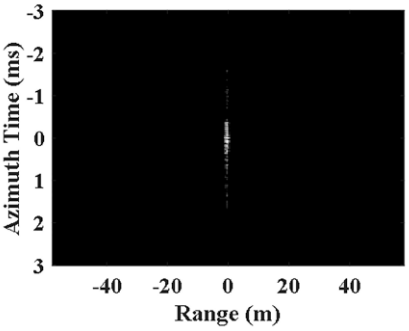

(c) MDL method

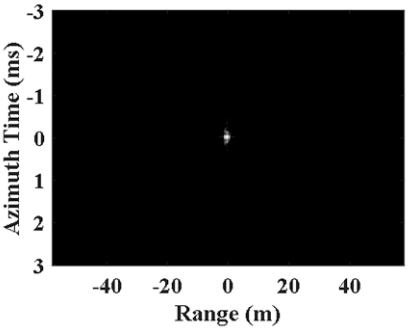

(d) Developed method

FIGURE 17. Point scatterer simulations of smearing suppression

Figure 18 shows a more complicated case involving two smeared regions with different initial phases that are superposed. The developed method still yields obvious residual energy. The reason for this phenomenon is that there is no notch in the time frequency analysis diagram, which is also why the developed method does not yield a better cancellation result in Figure 11.

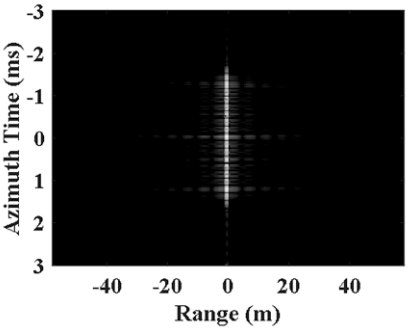

(a) Original image

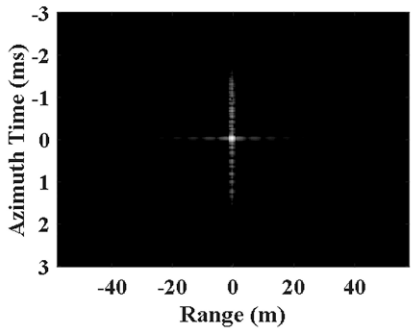

(b) Developed method

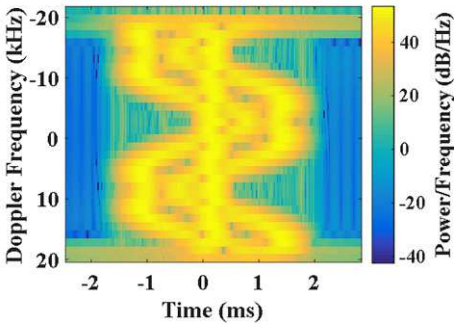

(c) Time frequency diagram of the middle line in (a)

FIGURE 18. Point scatterer simulations of multiple smeared regions.

B. ACTUAL MEASUREMENTS

Spotlight mode data from TerraSAR-X are used to validate the effectiveness of the developed method. The parameters of the SAR image are listed in Table Ⅱ.

TABLE Ⅱ
PARAMETERS OF THE PORT IMAGE

Symbol	Parameter Name	Value	Units
f_0	Radar frequency	9.65	GHz
θ_i	Incidence angle	37.85	deg
R_0	Slant range to center	635.15	km
B_r	Range bandwidth	300	MHz
B_a	Azimuth bandwidth	38.29	kHz
PRF	Pulse repetition frequency	4408.14	Hz
V_r	Equivalent speed	7074	m/s
T_a	Synthetic aperture time	6.96	s

There is a loading dock at the center of image, as shown in Figure 19, which causes smearing. With the developed method, multipath issues are effectively suppressed, and the resolution of the edges is not significantly affected. Furthermore, in the final result, three strong short lines remain along the dock. These lines are street lamps.

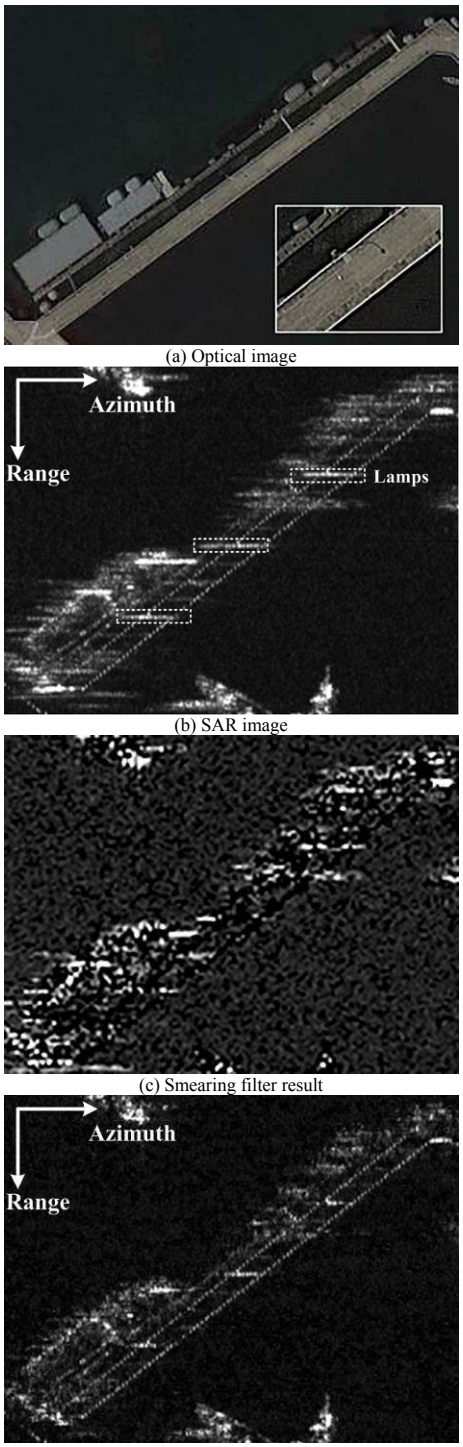

(a) Optical image

(b) SAR image

(c) Smearing filter result

(d) Suppression result

FIGURE 19. Loading dock. The lamps are retained, but the smearing is suppressed.

With the same parameters as in Table II, there are two vessels with heights of approximately 23 m at the port. The right vessel is influenced by smeared scatterers at the top side of the gunwale and near the water; as a result, the edge of the other side of the vessel is ambiguous. As shown in Figure 20, the border between the vessel and the dock can be distinguished after processing with the ideal filter, and the

mitigation effect is more obvious than those of both MDL and CF.

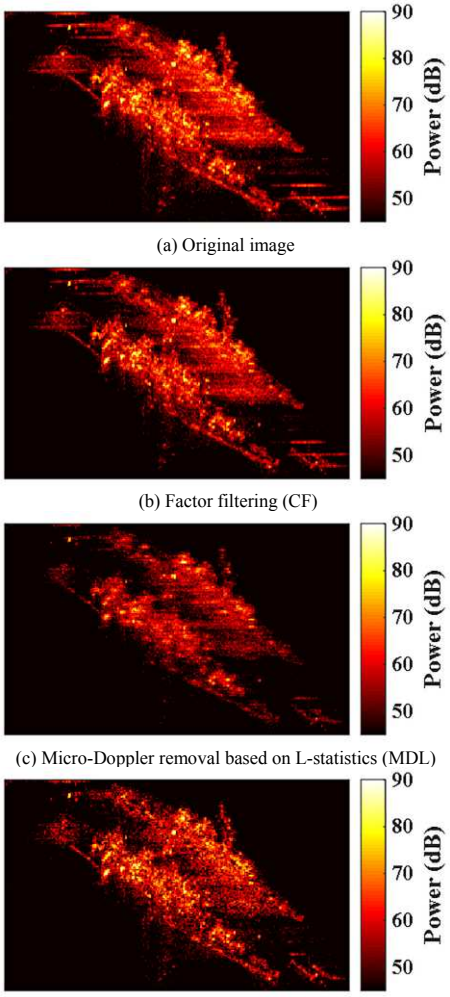

(a) Original image

(b) Factor filtering (CF)

(c) Micro-Doppler removal based on L-statistics (MDL)

(d) Developed method

FIGURE 20. Vessels (the horizontal direction is the range direction).

C. COMPUTATIONAL BURDEN

The CPU and processing software used in the experiments were an Intel Core i5-7200U at 2.5 GHz and MATLAB R2016b.

Three image processing experiments are performed in this article: (i) point scatterer simulations in Figure 17, (ii) the actual measurement of Lvshun in Figure 11, and (iii) actual sea port measurements, as shown in Figure 19 and Figure 20. The data scales and processing times of the different methods are shown in Table III. Notably, the developed method does not increase the computational burden but yields better performance compared to the other methods.

TABLE III
COMPUTATIONAL BURDEN

SN.	Scale	CF	MDL	Developed
i	256×256	0.40 s	1.33 s	0.46 s
ii	512×1024	28.92 s	42.73 s	35.40 s
iii	875×700	29.64 s	41.81 s	35.78 s

VI. CONCLUSION

In this paper, the smearing interference in SAR images of harbor scenes caused by varying multipath issues is analyzed, and an adaptive method is developed to detect and suppress the smearing effects.

According to the time-varying characteristic of blurring in harbor scenes, it is assumed that the Doppler spectra of false linear objects are discontinuous and undulating, and thus, the ICF filter can identify these spectra from the complex background. To avoid speckle noise interference, the threshold value of the ICF filter is set by studying the statistical properties of the image. Moreover, the energy of smearing can be estimated based on the ICF and the sliding narrowband filter results. Then, an ideal spatial filter is constructed to mitigate the defocused energy and maintain the resolution of the real targets.

Using TerraSAR-X data, some processing results for typical harbor scenes are provided. The smearing can be accurately separated from the background by the ICF filter, even if the shape of the real target is similar to that of the smeared region, and unwanted energy is suppressed with minimal resolution loss. As a result, the image quality is significantly improved.

However, the developed method cannot effectively improve well-focused multipath areas or several smeared overlapping objects because it is very difficult to find a clean notch in their Doppler spectra. Thus, other methods must be considered to solve such problems. According to (7) and (15), one possible solution is to select a higher beam position angle to observe the scene.

REFERENCES

[1] A. O. Knapskog, "Moving targets and multipath in SAR images of harbour scenes," in *European Conference on Synthetic Aperture Radar VDE*, Nuremberg, Germany, 2012, pp. 547-550.

[2] A. O. Knapskog, S. Brovoll, and B. Torvik, "Characteristics of ships in harbour investigated in simultaneous images from TerraSAR-X and PicoSAR," in *IEEE Radar Conference IEEE*, Washington, DC, USA, 2010, pp. 422-427.

[3] T. Sparr, "Moving target motion estimation and focusing in SAR images," in *IEEE International Radar Conference*, Arlington, VA, USA, 2005.

[4] D. Yan *et al.*, "Multipath ghosts location and sub-aperture based suppression algorithm for TWIR," in *IEEE Radar Conference*, 2016, pp. 1-4.

[5] Gennarelli, Gianluca, and F. Soldovieri, "Multipath Ghosts in Radar Imaging: Physical Insight and Mitigation Strategies," *IEEE J. Sel. Topics Appl. Earth Observ. Remote Sens.*, vol. 8, no. 3, pp. 1078-1086, Mar. 2015.

[6] M. Leigsnering *et al.*, "Multipath Exploitation and Suppression for SAR Imaging of Building Interiors: An overview of recent advances," *IEEE Signal Processing Magazine*, vol. 31, no. 4, pp. 110-119, Jun. 2014.

[7] I. de Arriba-Ruiz, F. Pérez-Martínez, and J. M. Muñoz-Ferreras, "Time-reversal-based multipath mitigation technique for entropy minimization of SAR images," in *IET Sensor Signal Processing for Defence*, London, UK, 2011, pp. 1-5.

[8] D. A. Garren *et al.*, "Image preconditioning for a SAR image reconstruction algorithm for multipath scattering," in *IEEE International Radar Conference*, Arlington, VA, USA, 2005, pp. 300-305.

[9] Y. Zhang *et al.*, "The Characteristics of the Multipath Scattering and the Application for Geometry Extraction in High-Resolution

SAR Images," *IEEE Trans. Geosci. Remote Sens.*, vol. 53, no. 8, pp. 4687-4699, Mar. 2015.

[10] X. Chen, W. Chen, "Multipath ghost elimination for through-wall radar imaging," *IET Radar, Sonar & Navigation*, vol. 10, no. 2, pp. 229-310, Feb. 2016.

[11] O. Biallawons, H. G. Ender, "Multipath Detection by Using Space-Space Adaptive Processing (SSAP) with MIMO Radar," in *2018 International Conference on Radar (RADAR)*, Brisbane, QLD, Australia, 2018, pp. 27-31.

[12] J. Liu *et al.*, "First-Order Multipath Ghosts' Characteristics and Suppression in MIMO Through-Wall Imaging," *IEEE Geoscience and Remote Sensing Letters*, vol. 13, no. 9, pp. 1315-1319, Jul. 2016.

[13] D. Sasakawa *et al.*, "Evaluation of fast human localization and tracking using MIMO radar in multi-path environment," in *2016 IEEE 27th Annual International Symposium on Personal, Indoor, and Mobile Radio Communications (PIMRC)*, Valencia, Spain, 2016.

[14] W. H. Munk, "Origin and generation of waves," in *Coastal Engineering Proceedings*, New York, USA, 1950.

[15] K. Hasselmann *et al.*, "Theory of synthetic aperture radar ocean imaging: A MARSEN view," *Journal of Geophysical Research: Oceans*, vol. 90, no. C3, pp. 4659-4686, May. 1985.

[16] G. G. Stokes, "On the theory of oscillatory waves," *Transactions of the Cambridge Philosophical Society*, vol. 8, pp. 441-455, 1847.

[17] W. J. Pierson, L. Moskowitz, "A proposed spectral form for fully developed wind seas based on the similarity theory of S. A. Kitaigorodskii," *Journal of Geophysical Research Atmospheres*, vol. 69, no. 24, pp. 5181-5190, Dec. 1964.

[18] S. T. Mathews, "A critical review of the 12th ITTC wave spectrum recommendations," in *International Towing Tank Conference*, Hamburg & Berlin, Germany, 1972, pp. 973-987.

[19] M. I. Skolnik, "Sea clutter" in *Radar Handbook*, 3th ed. USA: Mcgraw-Hill Publ. Comp., 2008, ch. 15, sec. 2, pp. 15.3-15.7.

[20] C. Wu, K. Y. Liu, M. Jin, "Modeling and a Correlation Algorithm for Spaceborne SAR Signals," *IEEE Transactions on Aerospace and Electronic Systems*, vol. AES-18, no.5, pp. 563-575, Sep. 1982.

[21] H. Kuang, J. Chen, W. Yang, and W. Liu, "An improved imaging algorithm for spaceborne MAPs sliding spotlight SAR with high-resolution wide-swath capability," *Chin. J. Aeronaut.*, vol. 28, no. 4, pp. 1178-1188, Aug. 2015.

[22] L. Stankovic *et al.*, "Micro-Doppler Removal in the Radar Imaging Analysis," *IEEE Transactions on Aerospace & Electronic Systems*, vol.49, no. 2, pp. 1234-1250, April, 2013.

[23] G. Gennarelli *et al.*, "Comparative Analysis of Two Approaches for Multipath Ghost Suppression in Radar Imaging," *IEEE Geosci. Remote Sens. Lett.*, vol. 13, no. 9, pp. 1226-1230, Jun. 2016.

[24] K. W. Hollman, K. W. Rigby and M. O'Donnell, "Coherence factor of speckle from a multi-row probe," in *IEEE Ultrasonics Symposium*, Caesars Tahoe, NV, USA, 1999, pp. 1257-1260.

[25] C. Oliver and S. Quegan, "Single-channel image types and speckle," in *Understanding Synthetic Aperture Radar Images*. London, England: Artech House, 2004, ch. 4, sec. 3, pp. 84-93.

[26] C. H. Seng *et al.*, "Probabilistic fuzzy image fusion approach for radar through wall sensing," *IEEE Trans. Image Process.*, vol. 22, no. 12, pp. 4938-4951, Aug. 2013.